

# Pure angular momentum generator using a ring resonator

Y. F. Yu<sup>1,2</sup>, Y. H. Fu<sup>1</sup>, X. M. Zhang<sup>3</sup>, A. Q. Liu<sup>1\*</sup>, T. Bourouina<sup>2</sup>, T. Mei<sup>1</sup>, Z. X. Shen<sup>4</sup>,  
and D. P. Tsai<sup>5</sup>

<sup>1</sup>*School of Electrical & Electronic Engineering, Nanyang Technological University, 639798, Singapore*

<sup>2</sup>*Ecole Supérieure d'Ingénieurs en Electronique et Electrotechnique (ESIEE), University of Paris East, 93162, France*

<sup>3</sup>*Department of Applied Physics, Hong Kong Polytechnic University, Hung Hom, Kowloon, Hong Kong S.A.R., China*

<sup>4</sup>*School of Physical & Mathematical Sciences, Nanyang Technological University, 639798, Singapore*

<sup>5</sup>*Department of Physics, National Taiwan University, Taipei, 10617, Taiwan*

\*[eaqliu@ntu.edu.sg](mailto:eaqliu@ntu.edu.sg)

**Abstract:** This paper reports a pure angular momentum generator using a ring resonator surrounded by a group of nano-rods. The evanescent waves of the circulating light in the ring are scattered by the nano-rods and generate a rotating electromagnetic field, which has only angular momentum but no linear momentum along the axis of rotation. The angular order is determined by the difference between the order of Whispering Gallery mode and the number of the rods, the rotating frequency is equal to the light frequency divided by the angular order. The maximum amplitude of the rotating electromagnetic fields can be 10 times higher than the amplitude of the input field when there are 36 rods ( $R_{\text{rod}} = 120$  nm,  $n_r = 1.6$ ). The pure angular momentum generator provides a new platform for trapping and rotation of small particles.

©2010 Optical Society of America

**OCIS codes:** (999.9999) Optical angular momentum; (130.3120) Integrated optics devices; (020.7010) Laser trapping; (170.4520) Optical confinement and manipulation

---

## References and links

1. J. H. Poynting, "The wave motion of a revolving shaft, and a suggestion as to the angular momentum in a beam of circularly polarised light," Proc. R. Soc. Lond., A Contain. Pap. Math. Phys. Character **82**(557), 560–567 (1909).
2. R. A. Beth, "Mechanical detection and measurement of the angular momentum of light," Phys. Rev. **50**(2), 115–125 (1936).
3. L. Allen, M. W. Beijersbergen, R. J. C. Spreeuw, and J. P. Woerdman, "Orbital angular momentum of light and the transformation of Laguerre-Gaussian laser modes," Phys. Rev. A **45**(11), 8185–8189 (1992).
4. K. T. Gahagan, and G. A. Swartzlander, Jr., "Optical vortex trapping of particles," Opt. Lett. **21**(11), 827–829 (1996).
5. Y. Torii, N. Shiokawa, T. Hirano, T. Kuga, Y. Shimizu, and H. Sasada, "Pulsed polarization gradient cooling in an optical dipole trap with a Laguerre-Gaussian laser beam," Eur. Phys. J. D **1**(3), 239–242 (1998).
6. X. P. Zhang, W. Wang, Y. J. Xie, P. X. Wang, Q. Kong, and Y. K. Ho, "Field properties and vacuum electron acceleration in a laser beam of high-order Laguerre-Gaussian mode," Opt. Commun. **281**(15-16), 4103–4108 (2008).
7. S. J. Parkin, G. Knöner, T. A. Nieminen, N. R. Heckenberg, and H. Rubinsztein-Dunlop, "Picoliter viscometry using optically rotated particles," Phys. Rev. E Stat. Nonlin. Soft Matter Phys. **76**(4), 041507 (2007).
8. J. Leach, H. Mushfique, R. di Leonardo, M. Padgett, and J. Cooper, "An optically driven pump for microfluidics," Lab Chip **6**(6), 735–739 (2006).
9. S. N. Khonina, V. V. Kotlyar, V. A. Soifer, M. Honkanen, J. Lautanen, and J. Turunen, "Generation of rotating Gauss-Laguerre modes with binary-phase diffractive optics," J. Mod. Opt. **46**, 227–238 (1999).
10. D. G. Grier, "A revolution in optical manipulation," Nature **424**(6950), 810–816 (2003).
11. K. Sueda, G. Miyaji, N. Miyana, and M. Nakatsuka, "Laguerre-Gaussian beam generated with a multilevel spiral phase plate for high intensity laser pulses," Opt. Express **12**(15), 3548–3553 (2004).
12. S. Franke-Arnold, J. Leach, M. J. Padgett, V. E. Lembessis, D. Ellinas, A. J. Wright, J. M. Girkin, P. Ohberg, and A. S. Arnold, "Optical ferris wheel for ultracold atoms," Opt. Express **15**(14), 8619–8625 (2007).
13. C. Y. Chao, W. Fung, and L. J. Guo, "Polymer microring resonators for biochemical sensing applications," IEEE J. Sel. Top. Quantum Electron. **12**(1), 134–142 (2006).
14. J. M. Choi, R. K. Lee, and A. Yariv, "Ring fiber resonators based on fused-fiber grating add-drop filters: application to resonator coupling," Opt. Lett. **27**(18), 1598–1600 (2002).

15. B. E. Little, J. S. Foresi, G. Steinmeyer, E. R. Thoen, S. T. Chu, H. A. Haus, E. P. Ippen, L. C. Kimerling, and W. Greene, "Ultra-compact Si-SiO<sub>2</sub> microring resonator optical channel dropping filters," *IEEE Photon. Technol. Lett.* **10**(4), 549–551 (1998).
16. Y. H. Ja, "Single-mode optical fiber ring and loop resonators using degenerate two-wave mixing," *Appl. Opt.* **30**(18), 2424–2426 (1991).
17. L. M. Tong, R. R. Gattass, J. B. Ashcom, S. L. He, J. Y. Lou, M. Y. Shen, I. Maxwell, and E. Mazur, "Subwavelength-diameter silica wires for low-loss optical wave guiding," *Nature* **426**(6968), 816–819 (2003).
18. C. Manolatou, M. J. Khan, S. H. Fan, P. R. Villeneuve, H. A. Haus, and J. D. Joannopoulos, "Coupling of modes analysis of resonant channel add-drop filters," *IEEE J. Quantum Electron.* **35**(9), 1322–1331 (1999).
19. Y. H. Ja, "Generalized theory of optical fiber loop and ring resonators with multiple couplers. 1: Circulating and output fields," *Appl. Opt.* **29**(24), 3517–3523 (1990).
20. J. A. Lock, "Contribution of high-order rainbows to the scattering of a Gaussian laser-beam by a spherical-particle," *J. Opt. Soc. Am. A* **10**(4), 693–706 (1993).
21. H. C. d. Hulst, *Light scattering by small particles* (Dover Publications, Inc., New York, 1981).

## 1. Introduction

It is well known that an electromagnetic field carries momentum. An interaction between field and mass is an exchange of momentum, either linear momentum or angular momentum. This exchange leads to the radiation force and the optical torque. For a circularly polarized light, the ratio of angular momentum to linear momentum is equal to  $\lambda/2\pi$  [1], where  $\lambda$  is the wavelength. The first experimental observation of the angular momentum in a polarized light was reported in 1936 [2]. The study of the angular momentum of Laguerre-Gaussian modes (LGMs) was reported at 1992 [3], which pointed out that for a light beam with  $l$ -order LGM the ratio of angular momentum to linear momentum is increased to  $l\lambda/2\pi$ . After this study, a number of applications using the angular momentum of the high-order LGM have been demonstrated, including the trapping of low refractive index spheres [4] and atoms [5], the acceleration of electrons [6] and the rotation of small particles [7,8]. Due to the existence of linear momentum, the samples in all these experiments are driven by radiation force and will move along the propagating direction of the light if there is no other balance force (e.g., optical tweezers [9]). To distinct between the angular momentum carried by the circularly-polarized light and that by the high-order LGM, the former is called *spin angular momentum* and the latter is *orbital angular momentum*. The generation of the orbital angular momentum is a key issue for many applications. For this purpose, the high-order LGMs are used extensively. They are usually generated by changing the phase structure of laser beam using binary-phase diffractive elements [10] and multilevel spiral phase plates [11]. It can also be generated by spatial light modulators [12]. However, these methods need specific designs for each order of LGM, face complication in fabrications and require large free-space for the arrangement of optical components. It becomes really desirable to produce pure angular momentum, which carries only orbital angular momentum and has no linear momentum along the axis of rotation. This is beneficial to optical integration since it does not need additional trapping force for sample rotation.

On the other hand, ring resonators have been widely used for biomaterial sensing [13], optical filtering [14,15] and optical wave mixing [16] thanks to its merits such as high Q-factor, narrow linewidth and flexible free spectrum range (FSR). Many materials including polystyrene [13], silicon [17] and silica [15] are used for fabricating the ring resonators, which also provide us a large range of refractive index (1.5 – 3.5) for the design. This work will utilize the ring resonator structure to generate the pure angular momentum.

## 2. Theoretical analysis

The design of the pure angular momentum generator is shown in Fig. 1(a). It consists of a ring resonator, a waveguide coupler and a group of circularly-periodical nano-rods surrounding the ring. The parameters of the generator include the ring radius  $R_{ring}$ , the ring width  $W_r$ , the number of the nano-rods  $N$ , the rod radius  $R_{rod}$ , the waveguide width  $W_w$ , the refractive index  $n_r$ , the input wavelength  $\lambda$ , the gap between the ring and the rods  $G_{rr}$ , the gap between the waveguide and the rod  $G_{wr}$ . With these parameters, the external radius of the ring is  $R_e = R_{ring} + W_r/2$  and the internal radius of the ring is  $R_{in} = R_{ring} - W_r/2$ . The centers of rods are

positioned at  $(R_s, j\theta_0)$ , where  $R_s = R_e + G_{rr} + R_{rod}$ ,  $\theta_0 = 2\pi/N$ , and  $j = 1, 2, \dots, N$ . The gap between the waveguide and the ring is  $G = 2R_{rod} + G_{rr} + G_{wr}$  as shown in Fig. 1(b).

The light propagation in the generator includes two steps. First, the light is input from the waveguide and coupled into the ring resonator through the evanescent field [18]. When the wavelength of the introduced light coincides with the resonant mode of the ring, the circulating field in the ring is enhanced and the output field at the end of the waveguide is significantly decreased. Second, the evanescent wave of the confined light in the ring is scattered by the nano-rods and the scattered waves form an electromagnetic field inside the ring. The circulation of the light in the ring causes a rotation of the electromagnetic field.

### 2.1 Light coupling effect

Considering the coupling efficiency between the ring and the waveguide as shown in Fig. 2, the related parameters include the field loss on the ring  $\alpha$ , the propagation constant  $\beta$ , the coupling coefficient  $K$ , the intensity loss  $\gamma$ , the ring radius  $R_{ring}$ , and the gap between the ring and the waveguide  $G$ . When there is no rod in between the waveguide and the ring as shown in Fig. 2(a), the electric fields  $E_1$  and  $E_3$  represent the electric fields before and after the coupling region in the waveguide, respectively, and  $E_2$  and  $E_4$  stand for the electric fields before and after the coupling region on the ring, respectively. When the resonator is at resonance, the relative intensity of the circulating light in the ring can be written in terms of  $\alpha$ ,  $R_{ring}$  and  $\gamma$  as [19]

$$I_c / I_i = |E_4 / E_1|^2 = (1 - \gamma) / \left( 1 - (1 - \gamma) e^{-4\alpha\pi R_{ring}} \right). \quad (1)$$

When there is one rod in between the waveguide and the ring as shown in Fig. 2(b), the light is scattered to all directions by the rod [20], which increases the intensity loss from  $\gamma$  to  $\gamma'$  and the coupling coefficient  $K$  to  $K'$ . Based on Eq. (1), the relative circulating intensity on the ring is reduced when  $\gamma$  goes higher in the range of  $(0, 1)$ . An increase of the rod radius would cause higher intensity loss  $\gamma$  and thus lower relative circulating intensity  $I_c/I_i$ .

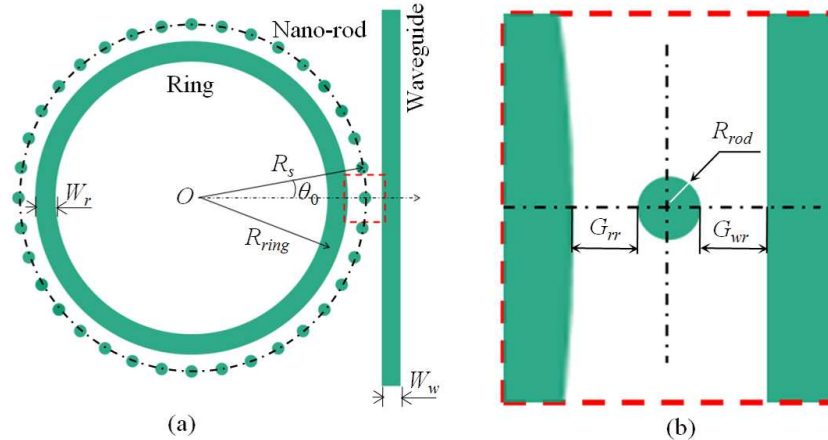


Fig. 1. (a) Design of the pure angular momentum generator using a ring resonator surrounded by a group of nano-rods; and (b) zoom view of the coupling region of the generator. The input light is coupled into the ring resonator to form a circulating wave, whose evanescent field is scattered by the nano-rods to construct an electrical field distribution inside the ring. With proper conditions, the electrical field inside the ring has a stable pattern and rotates with the circulation of the light confined in the ring.

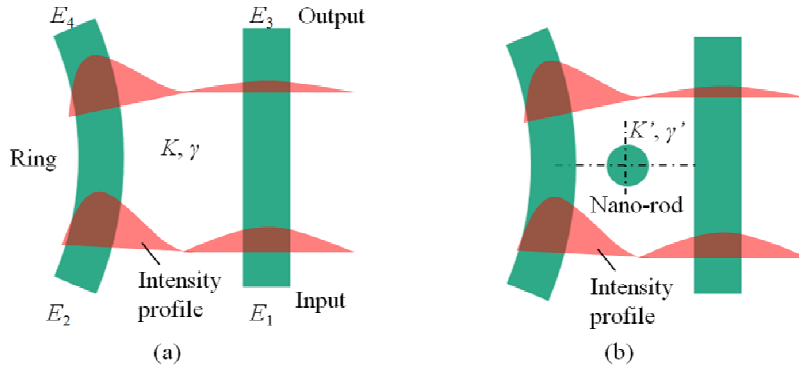


Fig. 2. (a) Waveguide-ring coupler without any rod; and (b) with a rod.

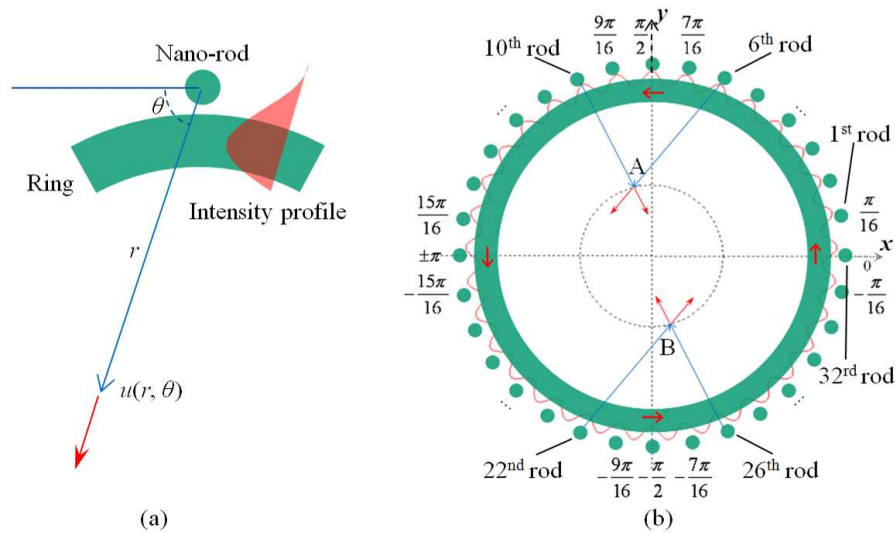


Fig. 3. (a) Light scattered by a single rod in the evanescent field of a ring; and (b) electrical field inside the ring when the number of rods  $N = 32$  and the order of WGM  $n = 33$ .

## 2.2 Generation of pure angular momentum

As can be observed from Fig. 2, the intensity profile of the circulating light on the ring has much wider distribution outside the ring than that inside the ring. Therefore, the nano-rods are designed to be positioned outside the ring so as to scatter more efficiently. At a point with arbitrary radius  $r$  and angle  $\theta$  in the polar coordinate system as shown in Fig. 3(a). The amplitude of the scattered light  $u(r, \theta)$  from one rod can be expressed as [21]

$$u(r, \theta) = s(\theta) \frac{e^{-ikr}}{ikr} u_o, \quad (2)$$

where  $\theta$  is the scattering angle,  $s(\theta)$  is the amplitude scattering factor,  $k$  is the wave vector, and  $u_o$  is the amplitude of the incident light (the evanescent wave). It is assumed that when viewed from any rod, the scattered lights from the neighboring rods are negligible as compared to the evanescent wave of the circulating light. Thus, the multiple scattering effects can be neglected. Based on the superposition principle and Eq. (2), the electromagnetic field at an arbitrary point A can be written as

$$u_A = \sum_{j=1}^N u_j^A = \sum_{j=1}^N s(\theta_j^A) \frac{\exp(-ikr_j^A)}{ikr_j^A} u_o^j, \quad (3)$$

where subscript  $j$  corresponds to the  $j^{\text{th}}$  rod, and  $\theta_j^A$  refers to the angle between the light propagation direction and the light scattering direction in the polar coordinate system that uses the  $j^{\text{th}}$  rod as the origin.

When the number of the rods  $N$  is equal to the WGM order  $n$  (i.e.,  $l = 0$ ), the electromagnetic field distribution inside the ring resonator becomes a series of concentric circles. Such distribution is close to the pattern of the 0th-order LGM in the plane perpendicular to the beam's propagation direction. When  $l = 1$ , the field distribution is same as the pattern of the 1st-order LGM in the plane perpendicular to the beam's propagation direction, and its rotation frequency  $f_r$  is equal to the light frequency. Detailed analyses and discussions of these two special cases are given in the appendix.

Similarly, when the difference between  $n$  and  $N$  is equal to  $l$  ( $l = |n - N|$ ), the electromagnetic field distribution inside the ring resonator has an  $l$ -fold rotational symmetry. This distribution is same as the pattern of the  $l$ -order (angular order) LGM. The corresponding rotating electromagnetic field has the rotation frequency  $f_r$ , which is equal to the light frequency  $f$  divided by the order  $l$  (that is,  $f_r = f/l$ ).

The linear momentum  $\mathbf{P}$  and angular momentum  $\mathbf{J}$  of the rotating electromagnetic field can be calculated as [3]

$$\bar{\mathbf{P}} = \bar{\mathbf{E}} \times \bar{\mathbf{B}}, \quad (4)$$

$$\bar{\mathbf{J}} = \epsilon_0 \int \bar{\mathbf{r}} \times (\bar{\mathbf{E}} \times \bar{\mathbf{B}}) d\bar{\mathbf{r}}, \quad (5)$$

where  $\epsilon_0$  is the vacuum permittivity. Since the light propagates only in the  $xy$ -plane, the linear momentum on the  $z$ -direction is zero (i.e., based on Eq. (4),  $P_z = 0$ ). Consider the rotation around the  $z$ -axis (at  $r_z = 0$ ), the angular momentum carried by the rotating electromagnetic field only exists in the  $z$  direction (i.e., based on Eq. (5),  $J_z \neq 0$ ,  $J_x = 0$ ,  $J_y = 0$ ). Thus, along the  $z$ -axis there is no linear momentum but only angular momentum. This is why the term 'pure angular momentum' is used in this paper.

### 3. Numerical results and discussions

Based on the finite difference time domain (FDTD) method, a series of rotating electromagnetic field are simulated, and the considered parameters include  $R_{ring}$ ,  $W_r$ ,  $N$ ,  $R_{rod}$ ,  $G_{rr}$ ,  $G_{wr}$ ,  $W_w$ ,  $n_r$  and  $\lambda$ . In order to simplify the simulation, the light coupling effect and the pure angular momentum generation will be discussed separately.

#### 3.1 Light coupling effect

Based on the Eq. (1), the relative intensity in the ring is directly related to the ring radius  $R_{ring}$ , the intensity loss  $\gamma$  and the ring's field loss  $\alpha$ . The intensity loss  $\gamma$  is associated with the  $R_{rod}$ ,  $G_{rr}$ ,  $G_{wr}$  and  $n_r$ , whereas the ring's field loss  $\alpha$  is associated with  $W_r$  and  $\lambda$ .

In order to study the influence of the nano-rod on the light coupling, the value of  $R_{ring}$  is set as a constant. Simulation shows that under the conditions  $|E_2| = |E_2'| = 0$  and  $|E_1| = |E_1'|$ , the coupler with a rod has higher coupling coefficient ( $K < K'$ ), which is concluded from the calculated results  $|E_4| < |E_4'|$  at the beginning as shown in Figs. 4(a) and 4(c). When there is a rod inside the coupler, the amplitude of circulating field is lower as shown in Figs. 4(b) and 4(d). The gap between the ring and the waveguide  $G$  is optimized for the highest relative circulating field ( $|E_4|/|E_1|$ ), and the optimized value varies with the wavelength  $\lambda$  as shown in Fig. 5(a). When the rod radius  $R_{rod}$  is increased, the relative circulating field ( $|E_4|/|E_1|$ ) is reduced. See Fig. 5(b) for the results at different gap ratios ( $G_{rr}/G_{wr}$ ). The other parameters are  $G = 0.2 \mu\text{m}$ ,  $n_r = 1.6$ ,  $\lambda = 619.1 \text{ nm}$  and  $W_r = W_w = 0.3 \mu\text{m}$ . The trend is changed from

decrease to increase after the critical value at  $R_{rod} = 0.1 \mu\text{m}$ , which is due to the overlap of the rod with the ring/waveguide. Further studies show that these conclusions are still correct when the refractive index is increased from 1.6 to 3.476.

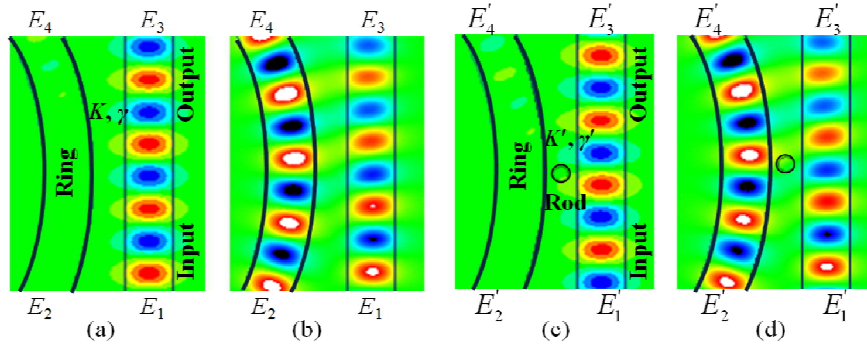


Fig. 4. The light coupling between the ring and the waveguide (a) without a rod and at the beginning; (b) without a rod and in the stable state; (c) with a rod and at the beginning; and (d) with a rod and in the stable state.

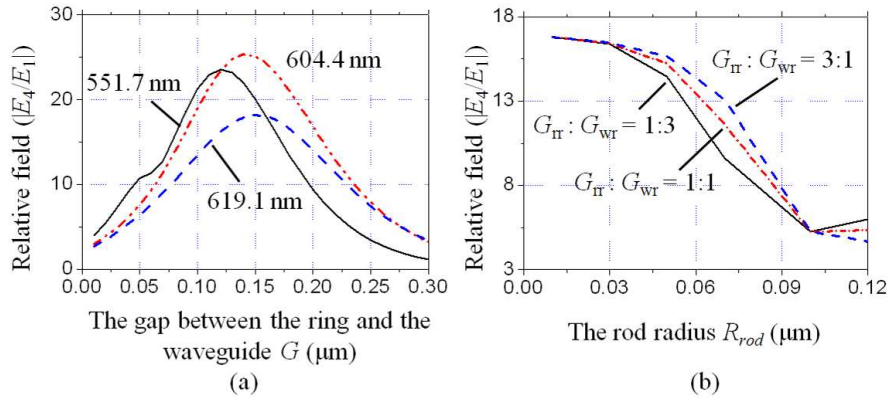


Fig. 5. The relative field as a function of (a) the gap between the ring and the waveguide at different wavelengths; and (b) the rod radius at different ratios of gaps.

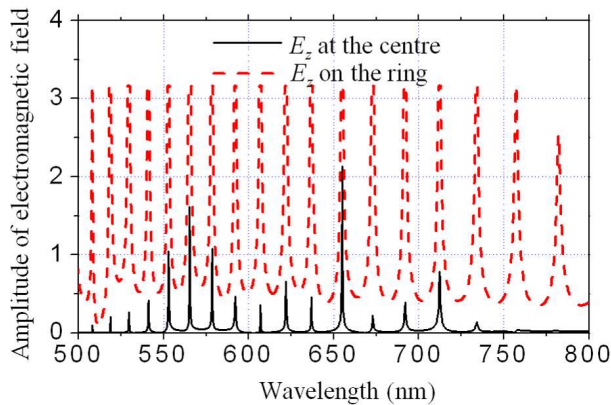


Fig. 6. The amplitude of field  $E_z$  versus the wavelength.

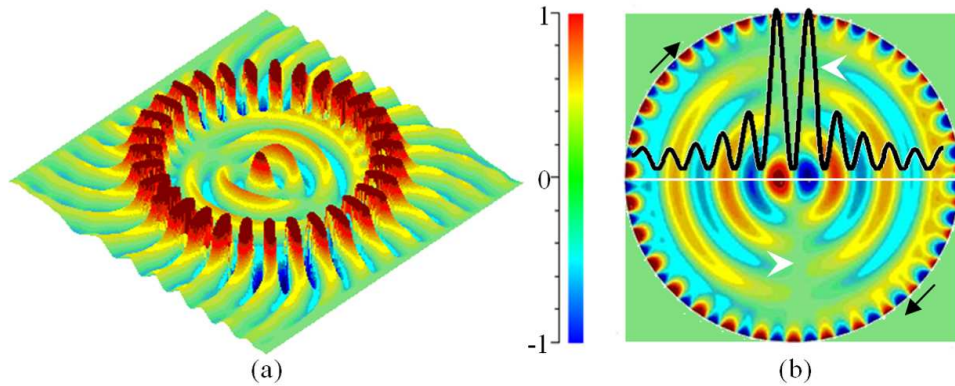


Fig. 7. The field distribution ( $E_z$ ) of the generator. (a) 3D view; and (b) top view inside the ring and the corresponding intensity distribution along the white line.

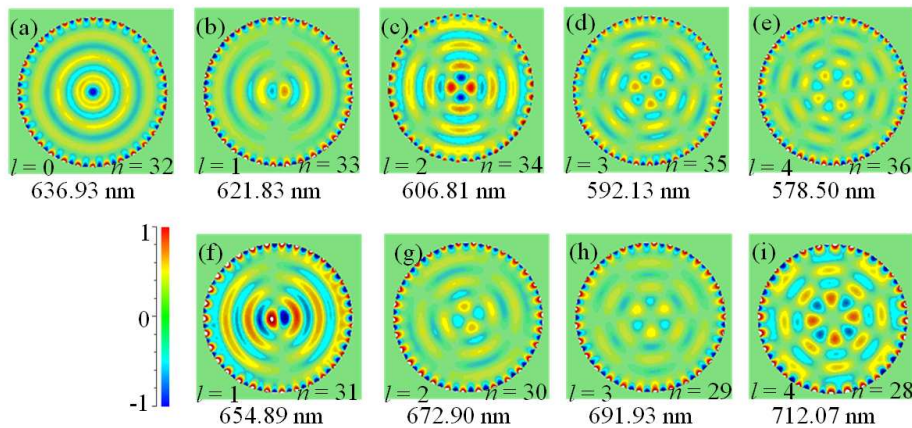


Fig. 8. The generated rotating electromagnetic fields. (a) The 0th order; (b) – (e) the 1st – 4th order in the short wavelength range; and (f - i) the 1st – 4th order in the long wavelength range. (Media 1), (Media 2)

### 3.2 Generation of pure angular momentum

For the pure angular momentum generator, when the parameters are  $N = 32$ ,  $R_{in} = 2.2 \mu\text{m}$ ,  $R_{out} = 2.5 \mu\text{m}$ ,  $R_{rod} = 0.1 \mu\text{m}$ ,  $G_{rr} = 0.1 \mu\text{m}$ ,  $n_r = 1.6$ ,  $W_r = W_w = 0.3 \mu\text{m}$ , the numerical results show that a series of WGMs have the wavelengths of 578.50 nm, 592.13 nm, 606.81 nm, 621.83 nm, 636.93 nm, 654.89 nm, 672.90 nm, 691.93 nm and 712.07 nm, which correspond to the order  $n$  from 36 to 28 as shown in Fig. 6. When the wavelength is 654.89 nm (corresponding to  $n = 33$ ), the electromagnetic field distribution inside the ring resonator has 1-fold symmetric structure as shown in Figs. 7(a) and 7(b), which agrees with the prediction in section 2.2. The corresponding circulating intensity in the ring is 75.4, which indicates that the field intensity decrease per circle is  $1/75.4$  (input energy/ total energy,  $\sim 1.3\%$ ) and it is negligible for the theoretical model. The field amplitude on the ring in Fig. 7(a) is set to 1 for the convenience of observation, and the black line in Fig. 7(b) is the intensity distribution along the white line.

When the wavelength is 636.93 nm, the order of WGM is 32, which is equal to the number of the rods  $N$ . The amplitude distribution of the electromagnetic field is a series of concentric circles as shown in Fig. 8(a). It matches with the analysis in section 2.2. Figures 8(b) – 8(e) show the 1st – 4th fold electromagnetic field distributions corresponding to the shorter

wavelengths and Figs. 8(f) – 8(i) show the electromagnetic field distributions corresponding to the longer wavelengths. Comparing Figs. 8(e) with 8(i), the radial orders (number of maxima along the radius) of the field distributions are different due to the wavelength difference even though the electromagnetic fields have same angular orders.

These electromagnetic fields not only have the  $l$ -fold rotational symmetric structure, but also have the rotation (except for  $l = 0$ ). The relationship of the rotation frequencies ( $f_r = f / l$ ) is also verified by the simulation results at different time frames (see videos related to Figs. 8(c) 8(f)) (Media 1), (Media 2). The rotation axis is perpendicular to the  $xy$ -plane and the rotation direction is indicated by white arrows in the Fig. 7(b). In this specific case, the rotation direction is opposite to the light circulation direction as indicated by the black arrows. Actually, the simulation results show that the rotation direction is opposite to the light circulation direction when  $n < N$  (i.e. Figs. 8(f) – 8(i)), and the same when  $n > N$  (i.e. Figs. 8(b) – 8(e)). In all cases, the rotating electromagnetic fields carry pure angular momenta.

### 3.3 Discussions

The generation efficiency  $\tau_{\pm l}$  of the  $l$ -order rotating electromagnetic field is defined as

$$\tau_{\pm l} = \left| \frac{E_r^{\pm l}}{E_{in}} \right|^2, \quad l = (0, 1, 2, \dots) \quad (6)$$

where  $E_{in}$  is the input field, the  $E_r^{\pm l}$  is the maximum amplitude of the  $l$ -order electromagnetic field, “+  $l$ ” corresponds to the condition  $n > N$  ( $l = n - N$ ), and “-  $l$ ” refers to  $n < N$  ( $l = N - n$ ). The rotating electromagnetic field is a combination of the scattering from the nano-rods, the evanescent field at the rods’ locations as well as the coupling effect of ring-waveguide coupler. Similar to the two steps mentioned above, the Eq. (6) can be rewritten as

$$\tau_{\pm l} = \left| \frac{E_c^{\lambda_n}}{E_{in}} \right|^2 \left| \frac{E_r^{\pm l}}{E_c^{\lambda_n}} \right|^2, \quad l = (0, 1, 2, \dots), \quad n = (1, 2, \dots) \quad (7)$$

where  $E_c^{\lambda_n}$  is the circulating field in the ring when the wavelength coincides with the  $n$ -order WGM. The first part on the left side of Eq. (7) is the same as the relative circulating intensity in Eq. (1). The second part presents the scattering efficiency of the group of nano-rods. Since  $E_{in}$  is set as 1, the generation efficiency of the  $l$ -order rotating electromagnetic field is the same as the maximum intensity of the  $l$ -order electromagnetic field. In the second step of the simulation, the intensity of the coupled light from the waveguide is set as 1, which means the intensity at the output of the waveguide is kept as zero. The gap between the waveguide and the ring is adjusted accordingly to maintain the coupling intensity independently of the circulating intensity on the ring.

The variable  $E_r^{\pm l}$  is associated with the order of WGM  $n$ . When  $n$  is increased, the corresponding wavelength  $\lambda_n$  is decreased for the same design, and the amplitude of the evanescent field around the ring resonator is reduced. Once the wavelength  $\lambda_n$  is smaller than 550 nm, the evanescent fields around the ring become very weak, causing a low electromagnetic field inside the ring ( $E_r^{\pm l} < 0.5$ ). In contrast, when  $n$  is decreased,  $\lambda_n$  goes up, and the radiation loss is enhanced. The solid line in Fig. 6 shows that when  $\lambda_n$  is longer than 750 nm, the radiation loss is dominated and the circulating field  $E_c^{\lambda_n}$  in Eq. (10) is reduced to a low level, which in turn causes the weak electromagnetic field inside the ring ( $E_r^{\pm l} < 0.5$ ). The wavelength range that has  $E_r^{\pm l} > 0.5$  decreases with the increasing of the number of the rods  $N$  and the refractive index  $n_r$ . For instance, when the  $n_r$  is increased to 3.476 ( $N = 28$ ), the range is narrowed down to only one wavelength at 1350 nm as shown in Fig. 9(a).

For the same design, different order numbers  $l$  correspond to different maximum amplitudes of the electromagnetic fields inside the ring. When the wavelength is increased

from 519.2 nm to 541.6 nm ( $n_r = 1.6$ ,  $N = 36$ ), the maximum amplitude of the electromagnetic field is decreased from 10 to 3.6, and most energy is scattered away rather than be confined inside the ring as shown in Fig. 9(e) – 9(f).

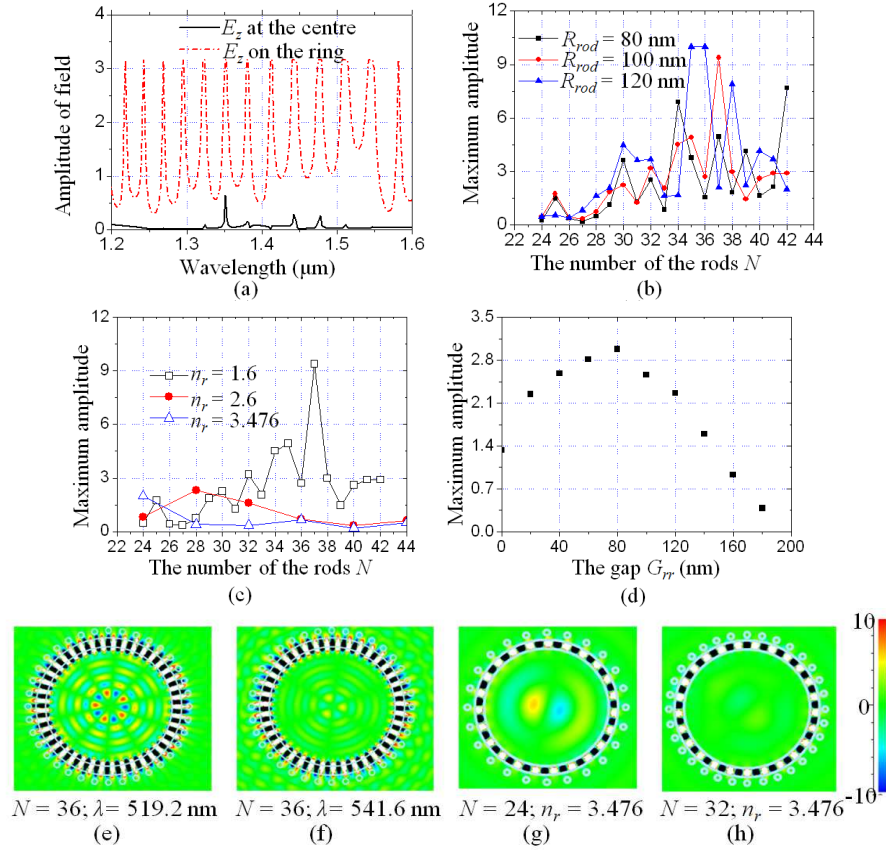


Fig. 9. (a) the amplitude of field  $E_z$  versus wavelength ( $N = 28$ ,  $n_r = 3.476$ ); the maximum amplitude inside the ring versus the number of the rods (b) with different  $R_{rod}$  ( $n_r = 1.6$ ), and (c) with different refractive indices ( $R_{rod} = 100$  nm); (d) the maximum amplitude inside the ring versus the gap  $G_{rr}$  ( $R_{rod} = 100$  nm,  $n_r = 1.6$ ); the field distribution when (e)  $N = 36$ ,  $\lambda = 519.2$  nm; (f)  $N = 36$ ,  $\lambda = 541.6$  nm; (g)  $N = 24$ ,  $n_r = 3.476$ ; and (h)  $N = 32$ ,  $n_r = 3.476$ .

For different  $N$ , the same  $l$  correspond different  $n$  (i. e.  $n = N \pm l$ ) and a wide range of  $\lambda_n$ . Since the wavelength affects the circulating intensity and the evanescent field, the amplitudes of the generated fields with same order numbers  $l$  cannot present the generation efficiency. To investigate the variations of the maximum value of all the maximum amplitudes  $E_r^{\pm l} |_{\max}$  with  $N$ , the rod  $R_{rod}$  as well as the refractive index  $n_r$  should be considered. The relationships are shown in Figs. 9(b) and 9(c). With  $n_r = 1.6$  and  $R_{rod} = 0.08 \mu\text{m}$ ,  $E_r^{\pm l} |_{\max}$  tends to increase when  $N$  goes from 24 to 37, and then decreases when  $N > 37$  (see Fig. 9 (b)). For different rod radii, the peak positions are different. The maximum value is 10 times higher than the amplitude of the input field when  $N = 36$ ,  $R_{rod} = 120$  nm,  $n_r = 1.6$ ,  $\lambda = 519.2$  nm,  $l = 5$ , circulating field  $E_c = 14.7$ . The field distribution is shown in Fig. 9(e). When  $n_r = 1.6$ , 2.6 or 3.476, the peak position appear at  $N = 37$ , 28 or 24, respectively (see Fig. 9(c)). After the peak position, the increase of  $N$  causes a reduction of  $E_r^{\pm l} |_{\max}$ . For example, when  $N$  is increased from 24 to 32 ( $n_r = 3.476$ ,  $l = 1$ ),  $E_r^{\pm l} |_{\max}$  is reduced from 1.9 to 0.2 as shown in Figs. 9(g) and 9(h).

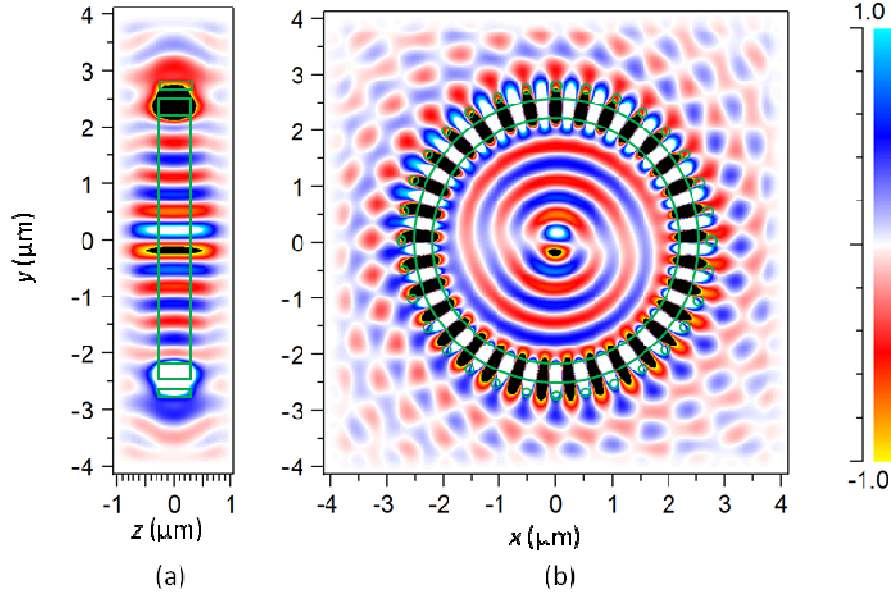


Fig. 10.  $E_z$  field contour map of the 3D simulation (a) cross section view at  $x = 0$ ; and (b) cross section view at  $z = 0$  for  $l = 1$ .

The gap between the ring and the rods  $G_{rr}$  also affects  $E_r^{\pm l}|_{\max}$ . An increase of  $G_{rr}$  causes a reduction of the scattering from each rod, whereas a decrease of  $G_{rr}$  results in higher field loss  $\alpha$ , which in turn decreases the circulating field on the ring. For  $R_{rod} = 100$  nm and  $n_r = 1.6$ , the optimized value is 80 nm as shown in Fig. 9(d).

When the structures have a limited height but are symmetric to the  $xy$ -plane ( $z = 0$ ), the electromagnetic field is also symmetric to this plane. In this case, the field has maximum amplitude in the same plane as shown in Fig. 10(a). In the  $xy$ -plane ( $z = 0$ ), the electromagnetic field distribution is same as previous presentation as shown in Fig. 10(b) and has no linear momentum in  $z$  direction. Assuming a particle has a small displacement from this plane, the gradient force will draw it back, like what happens in optical trapping. This means the generated electromagnetic field can stably trap small particles. The scattering light has a divergent angle in the vertical ( $z$ ) direction due to the small height (400 nm), and the divergent angle can be reduced by increasing the height.

#### 4. Conclusions

A pure angular momentum generator consisting of a ring resonator, a waveguide and a group of nano-rods is designed and analyzed. The numerical results show that a series of  $l$ -order rotating electromagnetic fields are generated when different resonant wavelengths are coupled into the generator. These fields have pure angular momenta but no linear momenta along the axis of rotation. Detailed studies on the influences of different structural parameters on the electromagnetic field have been conducted. The maximum amplitude of generated fields could be 10 times higher than that of the input field. The pure angular momentum generator overcomes the complication of linear momentum to the rotation of the small particles and provides a compact and flexible platform to study the rotational behaviors in micro-scale.

#### Appendix

Two special cases for  $l = 0$  and  $l = 1$  are studied here so as to exemplify the features of the electromagnetic field.

When  $n = N = 32$  (correspondingly  $l = 0$ ), the circumference of the ring is 32 times of the effective wavelength  $\lambda_{eff}$ , and thus the evanescent waves scattered by different rods ( $u_o^l$ ) have

same phases. Therefore, the electromagnetic field on a concentric circle of the ring should be exactly the same when observed from the position of any rod. In other words, the electromagnetic field on any concentric circle of the ring has a 32-fold rotational symmetry. In addition, it has mirror symmetry to any radial axis that passes one of the rods. With such a high level of symmetry, the electromagnetic field has little difference at different points on the concentric circle and thus presents to have a uniform distribution on the whole concentric circle. As a result, the electromagnetic field distribution inside the ring resonator becomes a series of concentric circles. Such distribution is close to the pattern of the 0th-order LGM in the plane perpendicular to the beam's propagation direction.

Considering another special case when  $l$  is 1 ( $l = n - N = 1$ , i. e.,  $n = 33$ , and  $N = 32$ ), there is a phase difference of  $\pi/16$  between the two evanescent waves scattered by the  $j^{\text{th}}$  rod and the  $(j + 1)^{\text{th}}$  rod. If the phase of the evanescent wave scattered by the 32nd rod is set as 0, the other phases of the evanescent waves scattered by the 1st to 31st rods are shown in Fig 3(b). Point A and point B are on the same concentric circle of the ring, and they are symmetrical to the origin. Based on Eq. (3), the electromagnetic fields at the points A and B can be expressed as

$$u_A = \sum_{j=1}^{32} u_j^A = \sum_{j=1}^{32} s(\theta_j^A) \frac{\exp(-ikr_j^A)}{ikr_j^A} u_o^j \quad \text{and} \quad u_B = \sum_{j=1}^{32} u_j^B = \sum_{j=1}^{32} s(\theta_j^B) \frac{\exp(-ikr_j^B)}{ikr_j^B} u_o^j. \quad (\text{A1})$$

Considering the contribution of the scattering from the 6th and 10th rods to point A, it has

$$u_6^A + u_{10}^A = s(\theta_6^A) \frac{\exp(-ikr_6^A)}{ikr_6^A} u_o^6 + s(\theta_{10}^A) \frac{\exp(-ikr_{10}^A)}{ikr_{10}^A} u_o^{10}. \quad (\text{A2})$$

The phase difference between the evanescent waves scattered by the  $j^{\text{th}}$  rod and the 32nd rod is  $j\pi/16$  ( $u_o^j = u_o^{32} \exp(i(j\pi/16))$ ), and then Eq. (A2) is expressed as

$$u_6^A + u_{10}^A = u_o^{32} \left[ s(\theta_6^A) \frac{\exp(-ikr_6^A)}{ikr_6^A} \exp\left(i\frac{6\pi}{16}\right) + s(\theta_{10}^A) \frac{\exp(-ikr_{10}^A)}{ikr_{10}^A} \exp\left(i\frac{10\pi}{16}\right) \right]. \quad (\text{A3})$$

Based on the geometrical relationship as shown in Fig. 3(b),  $r_6^A = r_{22}^B$ ,  $r_{10}^A = r_{26}^B$ ,  $\theta_6^A = \theta_{22}^B$ , and  $\theta_{10}^A = \theta_{26}^B$ . Then, Eq. (A3) can be rewritten as

$$\begin{aligned} u_6^A + u_{10}^A &= u_o^{32} \left[ s(\theta_{22}^B) \frac{\exp(-ikr_{22}^B)}{ikr_{22}^B} \exp\left(i\frac{-10\pi}{16}\right) + s(\theta_{26}^B) \frac{\exp(-ikr_{26}^B)}{ikr_{26}^B} \exp\left(i\frac{-6\pi}{16}\right) \right] \exp(i\pi) \\ &= (u_{22}^B + u_{26}^B) \exp(i\pi), \quad (\text{A4}) \end{aligned}$$

which means the contribution of the scattered lights from the 6th and 10th rods to point A is same as that from the 22th and 26th rods to point B, except for a  $\pi$  phase difference. Considering the rotational symmetry of the generator, the total electromagnetic fields at the points A and B should have a  $\pi$  phase difference ( $u_A = u_B \exp(i\pi)$ ), which means the electromagnetic field distribution inside the ring resonator is symmetric to the origin but has different directions. This distribution is same as the pattern of the 1st-order LGM in the plane perpendicular to the beam's propagation direction.

When the light on the ring propagates by  $\lambda_{\text{eff}}/32$ , the 0-phase rod and  $\pm\pi$  phase rod are shifted to the next rods, and the  $x$ -axis and  $y$ -axis have a  $\pi/16$  rotation around the  $z$ -axis. As a result, the electromagnetic field distribution inside the ring has a rotation of  $\pi/16$ . Therefore, the rotation frequency  $f_r$  is equal to the light frequency (that is,  $f_r = f$ ).

## **Acknowledgements**

This work was funded by the Environmental and Water Industry Development Council of Singapore, research project (Grant No. MEWR C651/06/171).